NJC

ROYAL SOCIETY OF CHEMISTRY

PAPER

View Article Online
View Journal | View Issue

Check for updates

Cite this: *New J. Chem.*, 2024, **48**, 19519

Determination of contact ion-pair formation in $CoCl_2$ aqueous, methanol, and ethanol dilute solutions by UV-vis and X-ray absorption spectroscopies†

Alessandro Tofoni, Matteo Busato,* Irene Rigacci, Mauro Giustini and Paola D'Angelo*

Received 11th September 2024,
Accepted 30th October 2024

DOI: 10.1039/d4nj03982c

rsc.li/njc

A detailed investigation on the coordination environment of the Co^{2+} ion has been carried out with the intent of quantifying the contact ion-pair formation in dilute (0.1 mol L^{-1}) $CoCl_2$ aqueous, methanol (MeOH), and ethanol (EtOH) solutions. An effective approach has been employed combining UV-vis measurements, X-ray absorption spectroscopy, and density functional theory (DFT). The $CoCl_2$ metal salt is fully dissociated in aqueous solution with the Co^{2+} cation first hydration shell formed by six water molecules arranged in an octahedral fashion. On the other hand, the chloride anion enters the Co^{2+} coordination sphere giving rise to ionic pairs in MeOH and EtOH solution due to the weaker solvation ability of these solvents. The Co–Cl distances are 2.34(2) and 2.26(3) Å in MeOH and EtOH solutions, respectively, as determined by extended X-ray absorption fine structure data analysis. In MeOH solution the dominant species is the octahedral $[CoCl(MeOH)_5]^+$ complex, while for EtOH the spectral evidence can be interpreted with an equilibrium between different four-fold metal-chloro species. Structural distortions in the coordination clusters have been evidenced by the X-ray absorption near-edge structure analysis aided by DFT optimizations and allowed us to rationalize the spectroscopic outcome of the UV-vis measurements. The adopted combined approach provided an all-around structural picture of the coordination complexes formed when the $CoCl_2$ salt is dissolved in solvents with different coordinating properties.

1 Introduction

Knowledge of the solvation structure around a metal ion in aqueous and organic media can disclose a fundamental understanding of the dissolution, transport, and thermodynamic properties of metal salt solutions. The solvation properties of donor solvents towards metal cations are usually studied focusing on the donor capabilities of the solvent and the coordinating structures of the cation that are influenced to some extent by the interactions among solvent molecules.[1,2] Conversely, little attention is usually devoted to the counterion. Despite this being justified for non-coordinating bulky anions with low charge density, the situation is different for anions with potential coordinating ability. In this case, the counterion can significantly alter the metal ion speciation through the formation of inner-sphere complexes, as previously demonstrated in several cases.[3–8] The quantification of ion–ion interactions is mandatory for the interpretation of the equilibrium and kinetic properties of chemical reactions involving metal centers and their coordination complexes. Understanding the anion exchange processes is also fundamental to elucidating the adsorption/desorption mechanism of a specific species from a solution phase to an extracting medium in the field of separation and waste fluid treatment. Nevertheless, detecting counterions entering a metal cation coordination sphere is often problematic due to the weak and transient nature of these interactions and the tendency to form solvent-separated species.[9]

The Co^{2+} ion is one of the most important cations in chemistry, physics, and biology, as it is widely diffused in catalytic systems;[10,11] $Co^{2+/3+}$ is a well-known redox couple,[12] and Co^{2+} centers are found in biologically relevant metalloproteins.[13] The coordination of Co^{2+} in solution has been demonstrated to be rather susceptible to conditions such as the solvent donor properties, solute concentration, temperature, and nature of the counterion. It is well known that the dissolution of Co^{2+} salts formed by weakly-coordinating anions such as ClO_4^-, $CF_3SO_3^-$ (TfO^-), and $(CF_3SO_2)_2N^-$ (Tf_2N^-) in relatively non-bulky solvents such as water, alcohols, dimethyl sulfoxide, and acetonitrile, results in

---

Department of Chemistry, Sapienza University of Rome, P.le Aldo Moro 5, 00185, Rome, Italy. E-mail: matteo.busato@uniroma1.it, p.dangelo@uniroma1.it

† Electronic supplementary information (ESI) available: Additional experimental details, additional XAS data and EXAFS analyses. See DOI: **https://doi.org/10.1039/d4nj03982c**

the formation of hexacoordinated octahedral complexes.[14–18] On the other hand, solutions of Co^{2+} halide salts can provide rather different geometries depending on the solvent donor properties.[19,20] The Co^{2+} coordination can also change at different temperatures, and this thermochromic character enhances the optical properties of Co^{2+} complexes.[21,22] In addition, aqueous Co^{2+} chloride complexes play a crucial role in cobalt transport and deposition in hydrothermal fluids, processing plants, and corrosion of Co-bearing alloys.[23] The solution chemistry of Co^{2+} in ion-containing media is also receiving renewed attention due to the high interest in determining the seawater speciation of its ^{60}Co radioactive isotope, which appeared in the sea of Japan as a sub-product of ^{127}Cs decay following the Fukushima–Daichii nuclear power plant accident in 2011.[24,25]

Aside from their practical significance, Co^{2+} halide solutions are ideally suited to retrieve fundamental insights on the different factors governing solvation equilibria through ligand competition, as the high affinity of the Co^{2+} ion for halide anions allows one to disclose metal–ligand interactions that are often not easily accessible in solution. Earlier structural investigations on $CoCl_2$ aqueous solutions evidenced the persistence of the octahedral hexaaquo complex even for salt concentrations up to 3.75 mol kg^{-1}.[26,27] On the other hand, contact ion-pair formation was observed to be more dependent upon temperature and salt concentration in methanol (MeOH) solution, as nuclear magnetic resonance (NMR) evidenced the formation of the monochloro octahedral complex $[CoCl(MeOH)_5]^+$ for temperatures below 15 °C and chloride concentrations up to 1.0 mol L^{-1}.[28,29] At the same time, the blue tetrahedral coordination becomes increasingly more important for higher temperatures. Inspection of the radial distribution function from X-ray diffraction (XRD) experiments on concentrated $CoCl_2$ solutions in water, MeOH, and ethanol (EtOH), showed that the Co^{2+} ion has four chloride nearest neighbors and forms a tetrachloro complex except for the aqueous solution, suggesting a relative coordinating ability towards the metal ion following the $H_2O > Cl^- > MeOH \simeq EtOH$ order.[26] Similar trends have been obtained by X-ray absorption spectroscopy (XAS) investigations about $CoBr_2$ in MeOH and EtOH solution, evidencing the existence of the $[Co(MeOH)_6]^{2+}$ and $[CoBr(MeOH)_5]^+$ complexes for salt concentrations of 0.2 and 3.8 mol L^{-1}, respectively, while $[CoBr_2\,(EtOH)_2]$ was detected as the dominant species in both 0.2 and 3.8 mol L^{-1} EtOH solutions.[19] More recent XAS investigations probed that ion association can occur even in $CoCl_2$ aqueous solution under extreme conditions, and the tetrahedral $[CoCl_2(H_2O)_2]$ and $[CoCl_4]^{2-}$ complexes predominate at temperatures up to 440 °C, constant pressure of 600 bar, and high salinity (0.0–6.0 mol kg^{-1} NaCl).[23] Other authors detected the presence of three complexes, namely $[Co(H_2O)_6]^{2+}$, the distorted $[CoCl(H_2O)_5]^+$ octahedron, and $[CoCl_4]^{2-}$, whose relative abundances were found to vary with HCl concentration for 0.0–11.0 mol L^{-1} HCl aqueous solutions.[30,31]

Herein, we present a study on dilute (0.1 mol L^{-1}) $CoCl_2$ solutions in water, MeOH, and EtOH. Co^{2+} salts with weakly coordinating anions (*i.e.*, NO_3^-, TfO^-, Tf_2N^-) were also analyzed for the sake of comparison. To this purpose we carried out a thorough experimental investigation combining UV-vis and XAS techniques. While the Co^{2+} ion is ideally suited for electronic absorption due to partially filled d-orbitals, XAS is the method of choice for the characterization of the nearest neighbors around an absorbing center in disordered systems and has been profitably used as a working horse for the study of metal ion solutions so far.[32–35] Advanced data analysis for both the X-ray absorption near-edge structure (XANES) and extended X-ray absorption fine structure (EXAFS) data, aided by density functional theory (DFT) simulations, have been employed, as the different energy regions of the XAS spectrum can provide complementary information on the three-dimensional arrangement of the scattering atoms.[17,36–38] This combined approach is intended to fully characterize the coordination sphere around the Co^{2+} ion and quantify the contact ion-pair formation between the metal cation and the chloride anions, with the general purpose of providing more fundamental insights into the structural properties of Co^{2+} aqueous and organic solutions in the presence of potentially coordinating ligands.

2 Materials and methods

2.1 Chemicals and sample preparation

Anhydrous $CoCl_2$, $Co(NO_3)_2$, $Co(TfO)_2$, and $Co(Tf_2N)_2$ were purchased from Merck (Milan, Italy), all with a stated purity of >99%, and used as received. 0.1 mol L^{-1} solutions were prepared by dissolving the appropriate amount of metal salt in Milli-Q water, anhydrous MeOH, and absolute EtOH. The resulting solutions were sonicated for about 10 minutes until homogeneous transparent samples were obtained. The list of the prepared samples is reported in Table S1 of the ESI.†

2.2 Electronic absorption measurements

Absorption spectra in the visible portion of the electromagnetic spectrum (Vis) were collected for 0.1 mol L^{-1} $CoCl_2$ and $Co(Tf_2N)_2$ solutions in water, MeOH, and EtOH. The measurements were carried out at room temperature with a Varian Cary 5E UV-vis-NIR spectrometer using quartz cells with 1.0 cm optical length for all samples except for $CoCl_2$ in EtOH. In this case, a 0.1 cm optical length was employed due to the higher sample absorbance. Absorbances were measured with an integration time of 0.1 s and a 0.5 nm interval in the 400–800 nm range. Linear background subtraction was applied to all spectra with the Spectra-Gryph software[39] and raw absorbances were converted to the molar extinction coefficient of the Co^{2+} ion.

2.3 XAS measurements

Co K-edge XAS spectra were collected on 0.1 mol L^{-1} $CoCl_2$ solutions in water, MeOH, and EtOH, as well as on $Co(NO_3)_2$ and $Co(TfO)_2$ in water and MeOH, respectively, at the Balder beamline of MAX IV Laboratory (Lund, Sweden).[40] Measurements were performed at room temperature in transmission geometry with a Si(111) double crystal monochromator, while the storage ring was operating at 3 GeV and the current was 400 mA. During the acquisition, the samples were kept in an *in situ* cell for liquids with Kapton windows and 3.0 mm spacers.

At least three spectra were collected and averaged for each sample. Data alignment was performed on the reference spectrum (Co foil). The XANES spectra were processed by fitting a linear background to the pre-edge region, which was subtracted from the entire spectrum, while the jump was normalized to unity with the post-edge asymptotic value chosen where the XAS oscillations were small enough to be negligible. Data reduction was performed with the ATHENA[41] and VIPER[42] software.

2.4 EXAFS data analysis

The analysis of the EXAFS region of the absorption spectra was carried out with the GNXAS code.[43,44] Amplitudes and phase shifts have been calculated from clusters with fixed geometry within the muffin-tin (MT) approximation. The MT radii were chosen to achieve a ∼20% overlap between adjacent MT spheres and were 1.60, 1.20, 0.90, 0.80, and 0.20 Å for Co, Cl, O, C, and H atoms, respectively. Advanced models for the exchange–correlation self-energy in the Hedin–Lundqvist (HL) scheme were used to account for the photoelectron inelastic losses in the final state.[45] Theoretical signals associated with n-body distribution functions were calculated following the multiple-scattering (MS) theory and summed to reconstruct the total theoretical contribution. Theoretical Co–O, Co–C, Co–H, and Co–Cl single-scattering (SS) signals were included to account for the coordinating solvent molecules and chloride anions. Note that, while the EXAFS technique has been proven to be sensitive towards ion–H pair distributions in aqueous solution,[16] the Co–H SS contribution has been found to have a negligible amplitude in MeOH due to the presence of only one hydrogen atom per solvent molecule. In addition, for the EtOH molecule, the Co–C signal is referred only to the C atom closer to the photoabsorber. Each two-body distribution was modeled as a Γ-like function depending on four structural parameters, namely the coordination number N, average distance R, Debye–Waller factor σ^2, and asymmetry index β, which were optimized during the fitting procedure to obtain the best agreement with the experimental data. O–Co–O and Cl–Co–O MS signals with 180° angle distributions were included in the fitting procedures in the case of six-fold coordination. Additional non-structural parameters were optimized, namely, E_0 which is the edge ionization energy, and the energy position and amplitude of the KM_1 and $KM_{2,3}$ double-electron excitation channels. The inclusion of the double-electron excitations allowed us to keep the amplitude reduction factor $S_0{}^2$ always constrained to 0.99.

2.5 XANES data analysis

The XANES region of the absorption spectra collected on the $CoCl_2$ solutions in MeOH and EtOH was analyzed with the MXAN code.[46–48] A full MS scheme was employed to calculate the X-ray absorption cross-section using a complex optical potential based on the MT approximation. The energy-dependent HL potential was used to calculate the real part of the exchange term, as it is known that the full complex HL potential leads to an over-damping of the cross-section at low energy.[49] To account for damping effects due to inelastic losses in a phenomenological manner, a Lorentzian function of energy-dependent width, Γ_{tot}, was used to convolve the theoretical spectra. This function is expressed as:

$$\Gamma_{\text{tot}} = \Gamma_{\text{c}} + \Gamma_{\text{mfp}} \quad (1)$$

where Γ_{c} represents the constant core–hole lifetime broadening and $\Gamma_{\text{mfp}}(E)$ models all intrinsic and extrinsic inelastic processes. $\Gamma_{\text{mfp}}(E)$ is an arctangent-like function equal to zero below the onset energy E_{s}, after which it increases according to the universal functional form of the photoelectron mean free path in solids, up to the value A_{s}. A fixed-width Gaussian convolution was performed to account for the experimental resolution.

In the MXAN procedure, each given structural model is optimized through a least-squares minimization over structural parameters of the residual function R_{sq}:

$$R_{\text{sq}} = \frac{\sum_{i=1}^{m} w_i \left[\left(y_i^{\text{th}} - y_i^{\text{exp}} \right) \varepsilon_i{}^{-1} \right]^2}{\sum_{i=1}^{m} w_i} \quad (2)$$

where m is the number of data points, y_i^{th} and y_i^{exp} represent the theoretical and experimental absorption cross-section, respectively, at each point m, ε_i takes into account the individual error of each point in the experimental spectrum, and w_i is a statistical weight. A constant value of $\varepsilon = 1.5\%$ was assumed for all spectra, while w_i was kept equal to 1 for all data points.

Every step of the minimization procedure includes a Monte Carlo refinement of the non-structural parameters Γ_{c}, Γ_{exp}, the Fermi energy level E_{F}, the threshold energy E_0, E_{s}, and A_{s}. An octahedral $[CoCl(MeOH)_5]^+$ cluster was employed as a structural model to fit the experimental data for the MeOH solution, while for the EtOH one the octahedral $[Co(EtOH)_6]^{2+}$ and the tetrahedral $[CoCl(EtOH)_3]^+$, $[CoCl_2\,(EtOH)_2]$, and $[CoCl_3\,EtOH]^{-1}$ clusters were employed (*vide infra*). The geometry of these clusters was previously optimized by DFT simulations, then all the Co–O and Co–Cl bond distances were fitted together with the bond angles involving the coordinating O and Cl atoms during the XANES analysis.

2.6 Computational details

DFT simulations were carried out for the octahedral $[CoCl(MeOH)_5]^+$ and $[Co(EtOH)_6]^{2+}$ and for the tetrahedral $[CoCl(EtOH)_3]^+$, $[CoCl_2(EtOH)_2]$, and $[CoCl_3EtOH]^-$ clusters with the ORCA 5.0.2 quantum chemistry code,[50] using the unrestricted formulation of the hybrid range-separated ωB97X-D3BJ functional together with the def2-TZVPD basis set.[51,52] Kohn–Sham equations were solved using the diagonalization-free KDIIS converger invoking the approximate second order self-consistent field (SOSCF) method at low orbital gradient values to speed up convergence.[53] The resolution of identity (RI) approximation with an automatically constructed auxiliary basis set,[54] corresponding to the AutoAux setting, was used to reduce the computational cost of Coulomb integrals, while Hartree–Fock exchange computations were treated with the chain-of-spheres exchange (COSX) approach.[55] Bulk solvent effects were implicitly accounted for using the conductor-like polarizable continuum model (CPCM) selecting the appropriate solvent for each cluster.[56] Vibrational analysis was carried out to ensure the absence of imaginary frequencies and that the obtained stationary points were true minima.

3 Results and discussion

3.1 Co^{2+} ion speciation by UV-vis spectroscopy

The partial filling of d-orbitals of the Co^{2+} ion provides a useful spectroscopic handle of its complexes, which is suitable for the determination of its speciation in solution. Absorption spectra in the Vis region have been recorded for the $CoCl_2$ aqueous, MeOH, and EtOH solutions, and compared with those obtained by dissolving the $Co(Tf_2N)_2$ salt in the same solvents. Tf_2N^- is a weakly-coordinating anion and provides, by comparison, insights about chloride anions entering the metal ion first coordination sphere. Visual inspection of the prepared samples shows that all aqueous solutions are pale pink to the naked eye, independently of the dissolved salt (Fig. S1, ESI†). Conversely, MeOH solutions are either pink or magenta, while the EtOH ones go from pink to deep blue depending on the dissolved salt. The Vis spectra collected on these samples are shown in Fig. 1. The shape and position of the absorption bands for the aqueous $CoCl_2$ (inset of Fig. 1) show the typical fingerprint of Co^{2+} octahedral coordination.[2,15,20–22,57–62] In addition, this spectrum shows the same band positions as that of the aqueous $Co(Tf_2N)_2$ solution. These findings suggest on the one hand the presence of the hexaaquo complexes in both water solutions, on the other one that the chloride anions do not enter the Co^{2+} ion first coordination sphere in dilute $CoCl_2$ aqueous solution.

The spectrum of the $CoCl_2$ solution in MeOH shows a similar shape as that of the aqueous sample in the 450–600 nm region, albeit with a small but detectable red-shift of the maximum position (inset of Fig. 1). Note that a slight red-shift as compared to the aqueous sample is also shown by the $Co(Tf_2N)_2$ solution in MeOH. This hypsochromic shift is due to the higher strength of the solvation of the ground state as compared with that of the excited state,[60,61] therefore the blue-shifted position of the aqueous spectra indicates that water is a stronger ligand towards the Co^{2+} ion as compared to MeOH. However, the spectrum of $CoCl_2$ in MeOH is red-shifted to the $Co(Tf_2N)_2$ one in the same solvent. This effect may arise from a certain amount of chloride anions entering the metal ion first solvation sphere, as the coordination of the weaker chloride ligand should produce a smaller crystal field splitting between the ground and the excited state. This picture is also supported by the higher absorption intensity of the $CoCl_2$ solution in MeOH. In fact, electronic transitions between states of the same multiplicity are dipole-forbidden and become partially allowed when deviations from the regular octahedral geometry occur.[2,20,57–59] Part of the transition intensity can be therefore caused by chloride anions in the Co^{2+} first coordination sphere that give rise to a non-centro-symmetric coordination geometry. This hypothesis is also supported by the appearance of additional contributions in the 600–750 nm spectral range in the case of the $CoCl_2$ salt, which are not present for the $Co(Tf_2N)_2$ solution in the same solvent. This band position suggests the presence of tetrahedral coordination.[20,58,59,62,63] However, it is worth stressing that much higher molar extinction coefficients are expected for the tetrahedral complexes, where no inversion center exists, as compared to the octahedral ones, because of a partial p-character in the electronic d–d transitions.[20,58–60] In light of this, the low intensity of the 600–750 nm bands subtends the presence of negligible amounts of tetraherdal complexes and the whole result is indicative of ion-pairing in the $CoCl_2$ MeOH solution, at variance with the aqueous one.

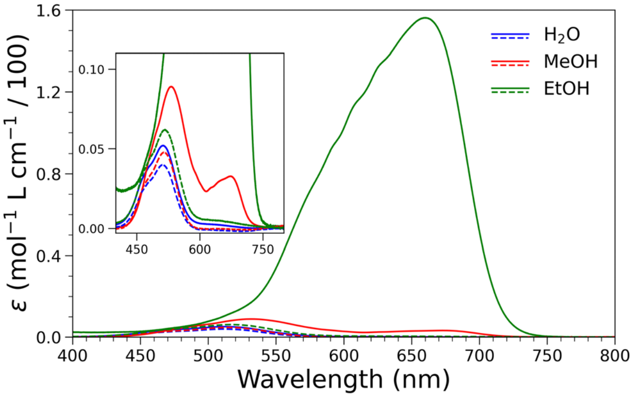

Fig. 1 Vis absorption spectra of the 0.1 mol L^{-1} $CoCl_2$ (full lines) and $Co(Tf_2N)_2$ (dashed lines) aqueous, MeOH, and EtOH solutions (inset: magnification of the 450–750 nm spectral region).

The absorption spectrum of the $CoCl_2$ solution in EtOH shows a wide and very intense band in the 500–750 nm range (Fig. 1), which is associated with the existence of a tetrahedral geometry of the Co^{2+} coordination complex.[20,58,59,62,63] Note that this band could hide the possible octahedron absorption in the 450–600 nm range due to the molar extinction coefficient being orders of magnitude higher for the tetrahedral case. On the other hand, dissolution of the $Co(Tf_2N)_2$ salt in EtOH leads to the octahedral coordination fingerprint, while no absorption bands are visible in the 450–600 nm range (inset of Fig. 1). This result suggests that a Co^{2+} tetrahedral complex predominates in EtOH solution, which is likely promoted by chloride anions able to replace EtOH molecules from the first solvation sphere. Further insights about the weaker donor capability of EtOH are given by the red-shifted maximum position of the $Co(Tf_2N)_2$ solution in EtOH as compared to the aqueous and MeOH ones.

The Vis data therefore evidenced a different speciation of the Co^{2+} ion due to a different extent of ion-pairing. The obtained trends can be explained by the donor properties of the solvents, which, according to their hard donor strength, follow the H_2O (24.7) > MeOH (16.7) > EtOH (14.0) sequence.[1,64–66] Quantifying the extent of such inner-sphere coordination and characterizing the structure of the formed complexes will be the subject of the following sections.

3.2 Co^{2+} ion speciation by XAS

Preliminary qualitative insights into the Co^{2+} ion's closest environment can be obtained from a comparison of the XAS data collected on the $CoCl_2$ aqueous, MeOH, and EtOH solutions (Fig. 2). An overall look at the XANES spectra outlines different features both in the white-line and higher energy region for the three samples (Fig. 2a). As the low-energy part of the absorption spectrum is highly sensitive towards the three-dimensional arrangement of the scattering atoms around the photoabsorber, this is a first clue of a different environment around the Co^{2+} ion in the three solvents. In particular, a progressive lowering of the white-line intensity, which has been previously associated with the interaction with halide anions,[23,67] is observed going from the aqueous to the MeOH and then to the EtOH solution. The pre-edge peak at about 7709 eV is worth special attention as this feature is due to the dipole-forbidden 1s → 3d transition. Still, the relaxation of the selection rules can occur from p–d orbital mixing granted by the lowering of the local symmetry around the photoabsorber, *i.e.*, deviations from regular octahedral coordination or removal of the inversion center.[68,69] The higher intensity of this pre-edge peak for the $CoCl_2$ solution in EtOH (inset of Fig. 2a) therefore supports a tetrahedral environment around the Co^{2+} ion in this medium, at variance with the aqueous and MeOH solutions, which show a less intense pre-edge transition. Notably, growth of the intensity of the shoulder at the rising edge at ~7717 eV, associated with the 1s → 4p transition, has been previously connected with the interaction between metals and halide ligands.[23,70,71] This feature is more intense for the EtOH solution and corroborates the higher extent of ion association in this medium.

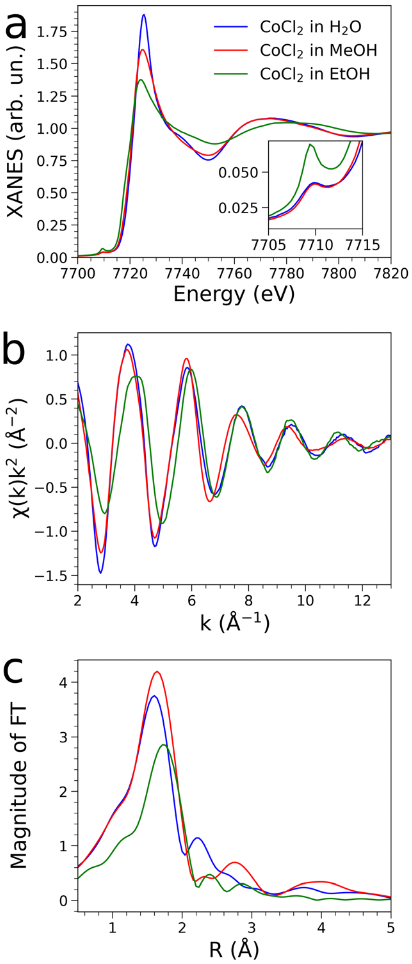

Fig. 2 Co K-edge (a) normalized XANES (inset: magnification of the pre-edge 1s → 3d transition), (b) EXAFS, and (c) non-phase shift-corrected FT experimental spectra collected on the 0.1 mol L^{-1} $CoCl_2$ aqueous, MeOH, and EtOH solutions.

Further insights about chloride anions entering the Co^{2+} first coordination sphere can be gained from the EXAFS data (Fig. 2b), given the higher sensitivity towards the first neighbor distances of this spectral region. The EXAFS oscillations of the aqueous and MeOH solutions are similar in the low-k region ($k < \sim 6$ Å^{-1}), while a mismatch in the phase is observed for higher k-values, where the phase shift due to different distances is more pronounced. In particular, the lower frequency of the MeOH solution indicates the presence of scattering centers at longer distances from the photoabsorber. This is compatible with the presence of chloride anions, which are expected to coordinate the Co^{2+} ion at longer distances as compared to the oxygen atoms of the water and MeOH molecules.[23,26] On the other hand, the much different amplitude and phase of the EtOH solution indicates a quite different coordination of the Co^{2+} ion in this solvent. Information on bond distances is made clearer by inspection of the FT signals in Fig. 2c. Here, one may observe that the position of the first peak, which is connected with the first-shell scattering atoms, follows the H_2O < MeOH < EtOH sequence. This result is compatible with an increasing number of chloride anion coordination following this trend. To corroborate these findings, in Fig. S2 (ESI†) we compare the XAS data collected for the $CoCl_2$ and $Co(NO_3)_2$ aqueous solutions. As can be observed, the XANES, EXAFS, and FT signals are almost identical. This indicates that in both solvents the Co^{2+} ion forms the same coordination complex and therefore no ionic pairs with the chloride ions are formed in the $CoCl_2$ aqueous solution. The XAS spectra of $CoCl_2$ and $Co(TfO)_2$ in MeOH solution are compared in Fig. S3 (ESI†). Clear differences are detected in the XANES region of the two spectra, while the FT first peak maximum of the $CoCl_2$ solution is found at higher distances. Altogether these findings suggest that in the former case chloride anions enter the metal first coordination sphere.

3.3 EXAFS results

A thorough analysis of the EXAFS data has been carried out to get a quantitative determination of the local structure around the Co^{2+} ion in the $CoCl_2$ aqueous, MeOH, and EtOH solution. As previously observed when the $CoCl_2$ salt is dissolved in water no ionic pairs are formed and the Co^{2+} inner hydration shell has an octahedral structure with six tightly bound water molecules.[16] In this case the EXAFS data have been analyzed including the Co–O and Co–H two-body signals in the theoretical calculation together with the linear O–Co–O three-body contribution. Least-squares fits of the EXAFS spectrum have been performed in the range k = 2.3–15.2 Å^{-1} and the minimization procedure has been applied to the whole set of structural and nonstructural parameters to improve, as far as

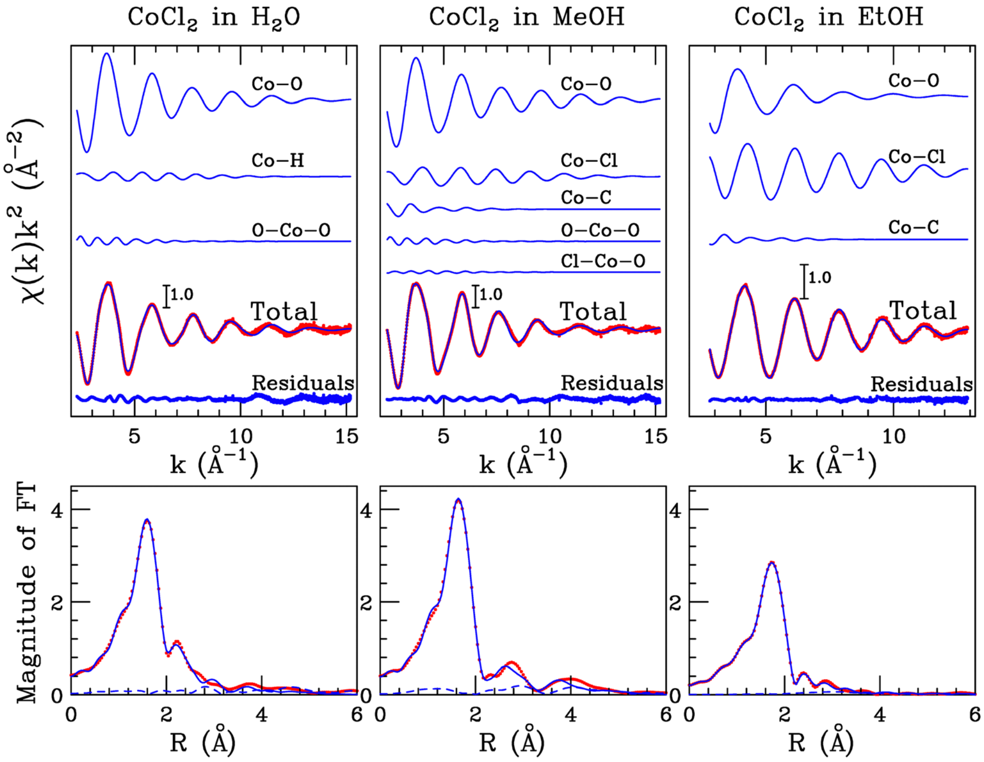

Fig. 3 Upper panels: analysis of the Co K-edge EXAFS spectra collected on the 0.1 mol L^{-1} $CoCl_2$ aqueous, MeOH, and EtOH solutions. From the top, the best-fit theoretical SS and MS signals are shown, together with the total theoretical contributions (blue lines) compared with the experimental data (red dots) and the resulting residuals (blue dots). Lower panels: non-phase shift-corrected FT's of the best-fit theoretical signals (blue line), of the experimental data (red dots), and of the residuals (blue dashed line).

possible, the agreement between calculated signals and experimental spectrum. In particular, we optimized four structural parameters for each single-shell contribution, and two additional structural parameters (the O–Co–O angle and its variance) for the three-body contribution. The best-fit analysis is shown in the upper left panel of Fig. 3. The first three curves from the top are the Co–O and Co–H first-shell SS contributions, and the O–Co–O MS signal associated with the linear configurations. The reminder of the figure shows the comparisons between the total theoretical contribution and the experimental spectrum, and the resulting residuals. Overall, the fitted EXAFS spectrum matches the experimental data very well and the reliability of the analysis is also proved by the nice agreement of the correspondent FT spectra shown in the lower panel of Fig. 3, calculated in the k range 2.3–12.0 $Å^{-1}$. The optimized structural parameters are listed in Table 1. Statistical errors on structural parameters have been estimated by looking at the confidence intervals in the parameters space as described elsewhere.[44,72] An average number of 6.0(3) neighboring oxygen atoms is determined at a 2.09(2) Å distance from the Co^{2+} ion (Table 1), which is fully compatible with previous results.[16–18] As far as the nonstructural parameters are concerned, the E_0 value was 1.5 eV above the first inflection point of the experimental spectrum, while S_0^2 was found to be equal to 0.99. Note that previous authors found that the Co^{2+} ion can give rise to different metal-chloro complexes in equilibrium, with relative abundance depending upon chloride concentration.[23,30,31,73,74] However, it was found that the naked Co^{2+} ion with no coordinated anions is predominant for concentrations corresponding to a 0.1 mol L^{-1} $CoCl_2$ solution, which is compatible with the hexaaquo complex detected in this work.[30,31]

Table 1 Best-fit structural parameters for the two-body distributions obtained from the EXAFS analysis of the 0.1 mol L^{-1} $CoCl_2$ aqueous, MeOH, and EtOH solutions. N is the coordination number, R the average distance, σ^2 is the Debye–Waller factor, and β is the asymmetry index. In the case of the EtOH molecule, Co–C is referred to as the C atom closer to the photoabsorber. Standard deviations are given in parenthesis

		N	R (Å)	σ^2 ($Å^{-2}$)	β
$CoCl_2$ in H_2O	Co–O	6.0(3)	2.09(2)	0.005(2)	0.0(1)
	Co–H	12.0(6)	2.77(3)	0.006(3)	0.0(2)
$CoCl_2$ in MeOH	Co–O	5.0(3)	2.09(2)	0.004(2)	0.2(1)
	Co–Cl	1.0(3)	2.34(2)	0.002(2)	0.4(1)
	Co–C	5.0(6)	3.23(5)	0.035(6)	0.9(3)
$CoCl_2$ in EtOH	Co–O	1.8(3)	2.04(3)	0.010(2)	0.0(1)
	Co–Cl	2.2(3)	2.26(3)	0.004(2)	0.9(1)
	Co–C	1.8(4)	3.42(5)	0.018(6)	0.0(3)

As previously mentioned the Vis data suggest that a certain number of chloride anions enter the first coordination sphere, while retaining an octahedral coordination in the $CoCl_2$ MeOH solution (Fig. 1). In this case the EXAFS data analysis has been carried out including the two-body Co–O and Co–C signals associated with the MeOH molecule, the SS Co–Cl contribution, together with the O–Co–O and O–Co–Cl three-body linear paths. The minimization procedure has been carried out in the range k = 2.3–15.2 Å^{-1} and the sum of the coordination numbers of the theoretical signals associated with the MeOH molecule and the chloride anion has been constrained to 6.0. The best-fit results are shown in the upper middle panel of Fig. 3. Starting from the top the Co–O, Co–Cl and Co–C two body signals and the O–Co–O and O–Co–Cl three-body contributions are shown together with the total theoretical curve compared with the experimental data, and the resulting residuals. The FT's of the theoretical and experimental signals calculated in the k range 2.3–12.0 Å^{-1} are shown in the lower panel. Also in this case the agreement between the theoretical and experimental data is excellent and the structural parameters obtained from the minimization procedure are listed in Table 1. In particular, the 1.0(3) chloride anion has been found to coordinate the Co^{2+} ion at a Co–Cl distance of 2.34(2) Å, while 5.0(3) first-shell MeOH molecules are found with Co–O and Co–C distances of 2.09(2) and 3.23(5), respectively. The EXAFS results suggest the formation of a $[CoCl(MeOH)_5]^+$ complex as previously found by NMR measurements on $CoCl_2$ solutions.[28,29] The Co–Cl distance is close to that determined by XRD measurements on a highly concentrated (3.91 mol kg^{-1}) solution in MeOH (2.30 Å).[26] The distribution of the different cobalt-chloro species formed in MeOH solution as a function of chloride concentration was also calculated by previous authors from their stability constants.[73] As a result, the mono-chloro complex is predominant for a 0.1 mol L^{-1} $CoCl_2$ concentration. This rules out that the coordination detected from our EXAFS analysis could derive from an equilibrium between different species and points at $[CoCl(MeOH)_5]^+$ as the dominant complex in dilute MeOH solution. This is at variance with what was previously found for a more concentrated $CoBr_2$ solution in MeOH compared to our case (0.2 mol L^{-1}), where a pure hexa-fold MeOH coordination was determined,[19] and can be reasonably explained by the higher coordination ability and smaller ionic radius of the Cl^- anion compared to the Br^- one.[75,76] To check the sensitivity of the EXAFS analysis and the reliability of our results, an additional fitting procedure has been carried out starting from a $[Co(MeOH)_6]^{2+}$ complex with no chloride ions in the inner coordination sphere. The results are shown in Fig. S4 (ESI†) and a clear mismatch between the theoretical and experimental spectra is observed in the high-k region (k > 6 Å^{-1}). The poor agreement in the higher k region can be explained by the lack of a contribution in the theoretical signal and this is also confirmed by the presence of a peak at about 2.0 Å in the residual FT shown in the lower panel of Fig. S4 (ESI†). Further proof of the reliability of our findings has been obtained by analyzing the EXAFS spectrum of $Co(TfO)_2$ in MeOH solution. In this case the minimization procedure has been performed starting from an octahedral geometry with six MeOH molecules in the Co^{2+} first coordination shell. The results of this analysis are shown in Fig. S5 (ESI†) and the excellent agreement between the experimental and theoretical data proves the validity of the suggested coordination model. The optimized structural parameters of both analyses are listed in Table S2 (ESI†) while the E_0 values were found to be 2.8 eV above the first inflection point of the experimental spectrum.

From the Vis data shown above, the existence of a tetrahedral coordination complex with chloride ions in the Co^{2+} first coordination sphere has been determined in the $CoCl_2$ EtOH solution (Fig. 1). Following this picture the EXAFS data have been analyzed starting from a tetrahedral model and only two SS Co–O and Co–C signals associated with the EtOH molecule and a SS Co–Cl contribution have been included in the calculation due to the lack of linear MS paths. Fitting procedures have been carried out in the k range 3.8–13.2 Å^{-1} by constraining the total coordination number of chloride anions and EtOH molecules to 4.0. The best-fit results are shown in the upper right panel of Fig. 3 where the two-body Co–O, Co–Cl and Co–C theoretical signals are plotted together with the total theoretical curve compared with the experimental spectrum and the corresponding residuals. Also in this case there is an excellent agreement between the theoretical and experimental spectra as also evident from the FT's calculated in the k range of 3.8–12.0 Å^{-1} and reported in the lower panel of Fig. 3. The optimized structural parameters are reported in Table 1. An average number of 2.2(3) and 1.8(3) chloride anions and MeOH molecules, respectively, have been determined, suggesting the existence of a $[CoCl_2(EtOH)_2]$ complex. The chloride anions coordinate at 2.26(3) Å and the EtOH molecules give rise to a Co–O distance of 2.04(3) Å. Note that the Co–O and Co–Cl distances are shorter than those obtained for the MeOH solution, suggesting an overall contraction of the bond distances for the four-fold coordination compared to the six-fold one. In this case E_0 was found to be 1.9 eV above the first inflection point of the experimental spectrum. The obtained coordination is also in line with that previously determined for a 0.2 mol L^{-1} $CoBr_2$ solution in EtOH, where the $[CoBr_2(EtOH)_2]$ species was detected.[19] This result is at variance with the MeOH case, where we found that the Cl^- anion coordinates the metal ion, while previous findings detected pure MeOH coordination for a 0.2 mol L^{-1} $CoBr_2$ solution.[19] Differently, Cl^- and Br^- both entering the metal ion coordination sphere in EtOH is indicative of the lower solvation capability of the EtOH molecule compared to the MeOH one. However, previous authors found that the distribution of Co^{2+} complexes in EtOH solution involves different metal-chloro species even for low chloride concentrations.[74] This suggests that, differently from the aqueous and MeOH cases, the coordination in EtOH solution could derive from an average between different equilibrium species rather than from a dominating complex, and this would also explain the fractional coordination numbers detected by EXAFS analysis (Table 1).

3.4 XANES results

At variance with the high-energy part of the absorption spectrum, in the XANES region there is a negligible Debye–Waller damping and this allows one to fully determine the three-dimensional arrangement of the scattering atoms around the photoabsorber. The sensitivity of XANES towards bond angles[38,77] has been exploited to better characterize the structure of the complexes formed in the $CoCl_2$ MeOH and EtOH solutions. The XANES data for the aqueous solution were not analyzed since in this case we detected a hexaaquo complex that has been extensively characterized previously.[17] Note that the presence of chloride ions in the Co^{2+} first coordination shell is expected to give rise to structural distortions from the ideal octahedral and tetrahedral geometries. In order to perform a quantitative analysis of the XANES spectra it is important to start from reliable structural models whose geometry can be refined on the basis of the experimental data. To this aim, we carried out DFT optimizations on different clusters for both the MeOH and EtOH solutions. For the MeOH case, we optimized only the $[CoCl(MeOH)_5]^+$ cluster as this was found to be the dominant species in a 0.1 mol L^{-1} $CoCl_2$ solution.[73] Differently, an equilibrium between different complexes, involving both the Co^{2+} ion merely solvated by the solvent and different metal-chloro species, was detected for the EtOH solution.[74] For this reason, we carried out DFT optimizations on the six-fold $[Co(EtOH)_6]^{2+}$ and on the four-fold $[CoCl(EtOH)_3]^+$, $[CoCl_2(EtOH)_2]$, and $[CoCl_3EtOH]^-$ clusters. Notably, the DFT calculations delivered distorted structures and the DFT-optimized clusters were used as starting models in the MXAN refinements of the XANES spectra. Minimization procedures were applied to all bond distances and angles involving the Co^{2+} ion and the results are shown in Fig. 4.

A very good agreement between the experimental and theoretical curves has been obtained for the $[CoCl(MeOH)_5]^+$ structure, whose theoretical spectrum is able to reproduce all the spectral features of the experimental data, as also shown by the residual function R_{sq}, which resulted in 1.1 (Fig. 4a). An exception is given by the bump at about ~20 eV above the edge in the experimental spectrum, which is not fully reproduced by the calculations. It has been demonstrated that this feature is due to the presence of the second solvation shell that has not been included in the analysis.[78,79] The optimized structural parameters for the $[CoCl(MeOH)_5]^+$ cluster are listed in Table 2. The determined Co–O and Co–Cl bond distances are in good agreement with those obtained from the EXAFS analysis (Table 1). The statistical errors in Table 2 were evaluated using the MIGRAD subroutine of the MINUIT library and stem from the correlation between the fitted parameters.[17,38,77] From the analysis of the XANES spectrum a small distortion from the ideal octahedral geometry has been observed. The optimized values of the $\theta_{O\text{–}Co\text{–}O}$ and $\theta_{Cl\text{–}Co\text{–}O}$ bond angles of the $[CoCl(MeOH)_5]^+$ cluster are lower than 180°, thus a bent configuration is obtained where the oxygen atoms of the MeOH molecules are placed below the equatorial plane of the octahedron (see the optimized cluster reported in Fig. 4a). This behavior is probably due to the repulsion between the equatorial MeOH molecules and the Cl^- anion. The distortion induced by the chloride ion can explain the trends of the Vis absorption band intensities (Fig. 1). This result is also in line with the determination of a distorted octahedral structure for the $[CoCl(H_2O)_5]^+$ cluster detected in aqueous solution at variable HCl concentration.[30]

For the EtOH case, the MXAN refinements starting from the octahedral $[Co(EtOH)_6]^{2+}$ cluster are shown in Fig. S6 (ESI†). As can be observed, this coordination completely fails in reproducing the experimental evidence, as also shown by the high residual function. This structure was employed as representative of the free Co^{2+} ion with no chloride coordination as from the Vis data of the $Co(Tf_2N)_2$ salt in EtOH (inset of Fig. 1) it is clear that the solvated ion gives rise to an octahedral coordination. This result clearly rules out the presence of free Co^{2+} ions in solution, while the XANES evidence supports that all the metal ions are coordinated by chloride anions. Given that the experimental Vis (Fig. 1) and XANES (Fig. 2a) data are compatible with a tetrahedral coordination, the mono-, di-, and tri-chloro cobalt species were modeled as the $[CoCl(EtOH)_3]^+$, $[CoCl_2(EtOH)_2]$, and $[CoCl_3EtOH]^-$ clusters, which were employed for the XANES analysis. The former structure shows the best agreement with the experimental data (Fig. 4b), while slightly higher values for the residual functions are obtained for the di- and tri-chloro clusters (Fig. 4c and d, respectively). Similarly to the MeOH case, the structures optimized by the MXAN fits are distorted, as the bond angles deviate from the 109.5° value of a regular tetrahedral coordination (Table 2). However, none of these clusters are capable of reproducing the XANES spectral features altogether, as slight mismatches can be clearly observed for both the intensity of the white-line region, the bump at ~20 eV above the edge, which is absent

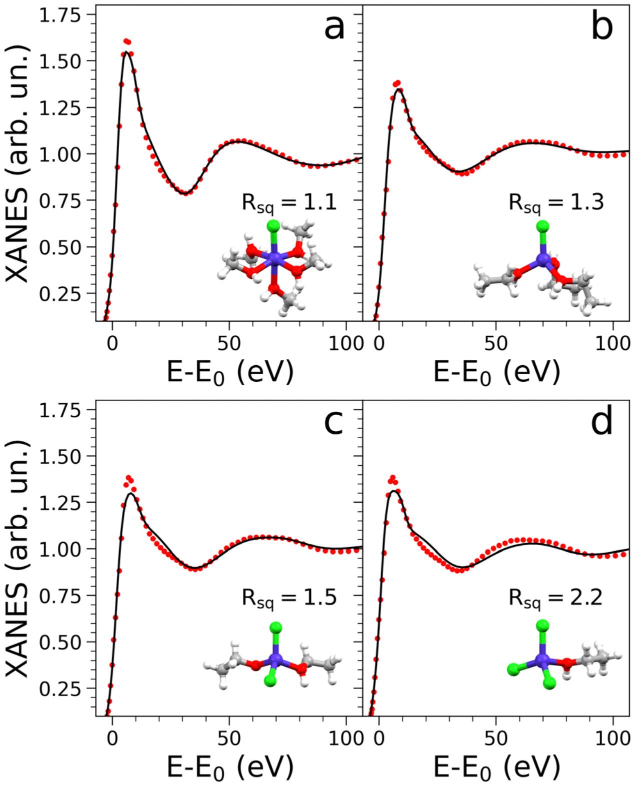

Fig. 4 Experimental Co K-edge XANES spectrum of (a) 0.1 mol L^{-1} $CoCl_2$ in MeOH (red dots) compared with the MXAN best-fit calculation (black full line) for the $[CoCl(MeOH)_5]^+$ cluster and experimental Co K-edge XANES spectrum of 0.1 mol L^{-1} $CoCl_2$ in EtOH (red dots) compared with the MXAN best-fit calculations for the (b) $[CoCl(EtOH)_3]^+$, (c) $[CoCl_2(EtOH)_2]$, and (d) $[CoCl_3EtOH]^{-1}$ clusters (black full lines). The residual functions R_{sq} are reported together with the optimized clusters (cobalt is purple, chlorine is green, oxygen is red, carbon is gray, and hydrogen is white).

Table 2 Best-fit structural parameters obtained from the analysis of the Co K-edge XANES experimental spectra collected on the 0.1 mol L^{-1} $CoCl_2$ MeOH and EtOH solutions. Standard deviations are given in parenthesis

	R_{sq}	$R_{Co–O}$ (Å)	$R_{Co–Cl}$ (Å)	$\theta_{O–Co–O}$ (°)	$\theta_{Cl–Co–O}$ (°)	$\theta_{Cl–Co–Cl}$ (°)
$[CoCl(MeOH)_5]^+$	1.1	2.10(3)	2.27(3)	168(4)	176(4)	—
$[CoCl(EtOH)_3]^+$	1.3	2.02(3)	2.29(3)	105(3), 96(3), 102(3)	113(3), 114(3), 124(3)	—
$[CoCl_2\ (EtOH)_2]$	1.5	2.06(3)	2.27(3)	102(3)	117(3)	113(3)
$[CoCl_3\ EtOH]^-$	2.2	2.10(3)	2.33(3)	—	103(3)	111(3), 103(3), 114(3)

in the experimental data, and the frequency of the first oscillation. This result is compatible with the presence of different species contributing to the average XANES signal and is at variance with the MeOH case, where the $[CoCl(MeOH)_5]^+$ cluster alone was able to give an excellent agreement between the theoretical and experimental evidence (Fig. 4a). Altogether these findings provide a detailed three-dimensional description of the Co^{2+} complex geometries and elucidated the impact of chloride anions entering these structures.

4 Conclusions

A detailed characterization of the Co^{2+} ion coordination in dilute $CoCl_2$ aqueous, MeOH, and EtOH solutions has been carried out with the intent of quantifying the contact ion-pair formation in the presence of chloride anions. We resorted to a combination of both experimental and theoretical techniques encompassing UV-vis spectroscopy measurements and advanced fitting procedures of XAS data, aided by DFT simulations. Equivalent solutions of Co^{2+} salts with weakly-coordinating counterions, *i.e.*, NO_3^-, TfO^-, and Tf_2N^-, were also analyzed for the sake of comparison.

Spectrophotometric measurements in the Vis region gave insights into the metal complex speciation. No ion-pair formation was observed in water and the Co^{2+} ion has been found to form an octahedral hexaaquo complex. Conversely, the presence of ion-pairs has been evidenced both in $CoCl_2$, MeOH and EtOH solutions due to the weaker coordinating ability of these solvents. In the former case, the presence of a distorted octahedral $[CoCl(MeOH)_5]^+$ complex has been clearly identified. In the latter, the spectral evidence can be interpreted with the presence of different mono-, di-, and tri-chloro cobalt species, with Co–Cl distances shorter than those observed in MeOH solution, rather than a dominating complex. The chloride inner-shell coordination induces distortions from the regular octahedral and tetrahedral coordinations in the two cases, and this explains the Vis and XANES results. The combined use of the UV-vis, EXAFS, and XANES spectroscopies allowed us to fully characterize the structural properties of dilute $CoCl_2$ aqueous, MeOH, and EtOH solutions and the same strategy can be used to shed light on the speciation of other systems containing transition metal ions.

Data availability

The data supporting this article have been included as part of the ESI.†

Conflicts of interest

There are no conflicts to declare.

Acknowledgements

The Balder beamline staff of MAX IV Laboratory is acknowledged for its support during synchrotron radiation beamtime. The authors acknowledge the European Union-NextGenerationEU under the Italian Ministry of University and Research (MUR), Network 4 Energy Sustainable Transition – NEST project – CUP B53C22004070006 and the Italian Ministry of University and Research (MUR) for the PRIN project ''MOF-MTM: tailoring Metal–Organic Frameworks for the direct Methane to Methanol conversion under mild conditions'' number 2022SFC459.

References

1 E. Kamieńska-Piotrowicz, *J. Chem. Soc., Faraday Trans.*, 1995, **91**, 71–75.
2 E. Kamieńska-Piotrowicz and J. Stangret, *J. Mol. Struct.*, 1998, **440**, 131–139.
3 P. D'Angelo, V. Migliorati, A. Gibiino and M. Busato, *Inorg. Chem.*, 2022, **61**, 17313–17321.
4 W. W. Rudolph and G. Irmer, *Dalton Trans.*, 2015, **44**, 295–305.
5 M. Duvail, A. Ruas, L. Venault, P. Moisy and P. Guilbaud, *Inorg. Chem.*, 2010, **49**, 519–530.
6 V. Migliorati, A. Gibiino, A. Lapi, M. Busato and P. D'Angelo, *Inorg. Chem.*, 2021, **60**, 10674–10685.
7 V. Migliorati, A. Serva, F. Sessa, A. Lapi and P. D'Angelo, *J. Phys. Chem. B*, 2018, **122**, 2779–2791.
8 V. Migliorati, A. Filipponi, F. Sessa, A. Lapi, A. Serva and P. D'Angelo, *Phys. Chem. Chem. Phys.*, 2019, **21**, 13058–13069.
9 G. R. Choppin, *J. Less Common Met.*, 1984, **100**, 141–151.
10 S. Liu, Y. He, W. Fu, J. Ren, J. Chen, H. Chen, R. Sun, Z. Tang, C. Mebrahtu and F. Zeng, *Appl. Catal., A*, 2024, **670**, 119549.
11 M. J. Earle, U. Hakala, B. J. McAuley, M. Nieuwenhuyzen, A. Ramani and K. R. Seddon, *Chem. Commun.*, 2004, 1368–1369.
12 M. D. Newton, *J. Phys. Chem.*, 1991, **95**, 30–38.
13 L. Rulíšek and J. Vondrášek, *J. Inorg. Biochem.*, 1998, **71**, 115–127.
14 Z. Luz and S. Meiboom, *J. Chem. Phys.*, 1964, **40**, 2686–2692.
15 Y. Inada, H. Hayashi, K.-i Sugimoto and S. Funahashi, *J. Phys. Chem. A*, 1999, **103**, 1401–1406.

16 P. D'Angelo, V. Barone, G. Chillemi, N. Sanna, W. Meyer-Klaucke and N. V. Pavel, *J. Am. Chem. Soc.*, 2002, **124**, 1958–1967.

17 P. D'Angelo, M. Benfatto, S. Della Longa and N. V. Pavel, *Phys. Rev. B*, 2002, **66**, 064209.

18 R. Spezia, M. Duvail, P. Vitorge, T. Cartailler, J. Tortajada, G. Chillemi, P. D'Angelo and M.-P. Gaigeot, *J. Phys. Chem. A*, 2006, **110**, 13081–13088.

19 M. Sano, T. Maruo, Y. Masuda and H. Yamatera, *J. Solution Chem.*, 1986, **15**, 803–809.

20 W. C. Nieuwpoort, G. A. Wesselink and E. H. A. M. van der Wee, *Recl. Trav. Chim. Pays-Bas*, 1966, **85**, 397–404.

21 S. Gadžurić, M. Vraneš and S. Dožić, *Sol. Energy Mater. Sol. Cells*, 2012, **105**, 309–316.

22 M. B. Vraneš, S. M. Papović and S. B. Gadžurić, *J. Solution Chem.*, 2019, **48**, 1364–1377.

23 W. Liu, S. J. Borg, D. Testemale, B. Etschmann, J.-L. Hazemann and J. Brugger, *Geochim. Cosmochim. Acta*, 2011, **75**, 1227–1248.

24 Y.-H. Koo, Y.-S. Yang and K.-W. Song, *Prog. Nucl. Energy*, 2014, **74**, 61–70.

25 D. Z. Caralampio, B. Reeves, M. R. Beccia, J. M. Martínez, R. R. Pappalardo, C. den Auwer and E. Sánchez Marcos, *Mol. Phys.*, 2019, **117**, 3320–3328.

26 D. L. Wertz and R. F. Kruh, *J. Chem. Phys.*, 1969, **50**, 4313–4317.

27 L. I. Katzin and E. Gebert, *J. Am. Chem. Soc.*, 1953, **75**, 2830–2832.

28 Z. Luz, *J. Chem. Phys.*, 1964, **41**, 1756–1762.

29 Z. Luz, *J. Chem. Phys.*, 1964, **41**, 1748–1755.

30 M. Uchikoshi and K. Shinoda, *Struct. Chem.*, 2019, **30**, 945–954.

31 M. Uchikoshi, *J. Solution Chem.*, 2018, **47**, 2021–2038.

32 A. Muñoz-Páez and E. Sánchez Marcos, in *Comprehensive Inorganic Chemistry II*, ed. J. Reedijk and K. Poeppelmeier, Elsevier, Amsterdam, 2nd edn, 2013, pp. 133–159.

33 A. Filipponi and P. D'Angelo, *XAS in Liquid Systems*, John Wiley & Sons, Ltd, 2016, ch. 25, pp. 745–771.

34 D. Roccatano, H. J. C. Berendsen and P. D'Angelo, *J. Chem. Phys.*, 1998, **108**, 9487–9497.

35 E. Burattini, P. D'Angelo, A. Di Cicco, A. Filipponi and N. V. Pavel, *J. Phys. Chem.*, 1993, **97**, 5486–5494.

36 M. Busato, G. Fazio, F. Tavani, S. Pollastri and P. D'Angelo, *Phys. Chem. Chem. Phys.*, 2022, **24**, 18094–18102.

37 M. Busato, A. Melchior, V. Migliorati, A. Colella, I. Persson, G. Mancini, D. Veclani and P. D'Angelo, *Inorg. Chem.*, 2020, **59**, 17291–17302.

38 P. D'Angelo and V. Migliorati, *J. Phys. Chem. B*, 2015, **119**, 4061–4067.

39 F. Menges, *Spectragryph – optical spectroscopy software, Version 1.2.15*, 2020, https://www.effemm2.de/spectragryph/.

40 K. Klementiev, I. Preda, S. Carlson, K. Sigfridsson and K. Norén, *J. Phys.: Conf. Ser.*, 2016, **712**, 012018.

41 B. Ravel and M. Newville, *J. Synchrotron Radiat.*, 2005, **12**, 537–541.

42 K. V. Klementev, *J. Phys. D: Appl. Phys.*, 2001, **34**, 209.

43 A. Filipponi, A. Di Cicco and C. R. Natoli, *Phys. Rev. B: Condens. Matter Mater. Phys.*, 1995, **52**, 15122–15134.

44 A. Filipponi and A. Di Cicco, *Phys. Rev. B: Condens. Matter Mater. Phys.*, 1995, **52**, 15135–15149.

45 L. Hedin and S. Lundqvist, *Solid State Phys.*, 1970, **23**, 1–181.

46 M. Benfatto, A. Congiu-Castellano, A. Daniele and S. Della Longa, *J. Synchrotron Radiat.*, 2001, **8**, 267–269.

47 M. Benfatto and S. Della Longa, *J. Synchrotron Radiat.*, 2001, **8**, 1087–1094.

48 M. Benfatto, S. Della Longa, E. Pace, G. Chillemi, C. Padrin, C. R. Natoli and N. Sanna, *Comput. Phys. Commun.*, 2021, **265**, 107992.

49 L. Hedin and B. I. Lundqvist, *J. Phys. C: Solid State Phys.*, 1971, **4**, 2064.

50 F. Neese, *Wiley Interdiscip. Rev.: Comput. Mol. Sci.*, 2022, **12**, e1606.

51 A. Najibi and L. Goerigk, *J. Chem. Theory Comput.*, 2018, **14**, 5725–5738.

52 A. Hellweg and D. Rappoport, *Phys. Chem. Chem. Phys.*, 2015, **17**, 1010–1017.

53 F. Neese, *Chem. Phys. Lett.*, 2000, **325**, 93–98.

54 G. L. Stoychev, A. A. Auer and F. Neese, *J. Chem. Theory Comput.*, 2017, **13**, 554–562.

55 F. Neese, F. Wennmohs, A. Hansen and U. Becker, *Chem. Phys.*, 2009, **356**, 98–109.

56 V. Barone and M. Cossi, *J. Phys. Chem. A*, 1998, **102**, 1995–2001.

57 O. G. Holmes and D. S. McClure, *J. Chem. Phys.*, 1957, **26**, 1686–1694.

58 S. Volkov, N. Buryak and O. Babushkina, *Theor. Exp. Chem.*, 1978, **13**, 423–427.

59 L. Rulíšek and Z. Havlas, *J. Chem. Phys.*, 2000, **112**, 149–157.

60 C. J. Thompson, K. P. Faherty, K. L. Stringer and R. B. Metz, *Phys. Chem. Chem. Phys.*, 2005, **7**, 814–818.

61 J. Amphlett, M. Ogden, W. Yang and S. Choi, *J. Mol. Liq.*, 2020, **318**, 114217.

62 J. Amphlett and S. Choi, *J. Mol. Liq.*, 2021, **332**, 115845.

63 H. A. Weakliem, *J. Chem. Phys.*, 1962, **36**, 2117–2140.

64 I. Persson, *Pure Appl. Chem.*, 1986, **58**, 1153–1161.

65 Y. Marcus, *Pure Appl. Chem.*, 1983, **55**, 977–1021.

66 E. Kamieńska-Piotrowicz, *Thermochim. Acta*, 2005, **427**, 1–7.

67 Y. Tian, B. Etschmann, W. Liu, S. Borg, Y. Mei, D. Testemale, B. O'Neill, N. Rae, D. M. Sherman, Y. Ngothai, B. Johannessen, C. Glover and J. Brugger, *Chem. Geol.*, 2012, **334**, 345–363.

68 D. Cabaret, A. Bordage, A. Juhin, M. Arfaoui and E. Gaudry, *Phys. Chem. Chem. Phys.*, 2010, **12**, 5619–5633.

69 T. Yamamoto, *X-Ray Spectrom.*, 2008, **37**, 572–584.

70 J. L. Fulton, S. M. Heald, Y. S. Badyal and J. M. Simonson, *J. Phys. Chem. A*, 2003, **107**, 4688–4696.

71 Y. Chen, J. Fulton and W. Partenheimer, *J. Solution Chem.*, 2005, **34**, 993–1007.

72 A. Filipponi, *J. Phys.: Condens. Matter*, 1995, **7**, 9343.

73 H. Doe and T. Kitagawa, *Inorg. Chem.*, 1982, **21**, 2272–2276.

74 S. Lechat, M. Khan, G. Bouet and F. Vierling, *Inorg. Chim. Acta*, 1993, **211**, 33–36.

75 P. D'Angelo, V. Migliorati and L. Guidoni, *Inorg. Chem.*, 2010, **49**, 4224–4231.

76 V. Migliorati, F. Sessa, G. Aquilanti and P. D'Angelo, *J. Chem. Phys.*, 2014, **141**, 044509.

77 R. Sarangi, M. Benfatto, K. Hayakawa, L. Bubacco, E. I. Solomon, K. O. Hodgson and B. Hedman, *Inorg. Chem.*, 2005, **44**, 9652–9659.

78 P. D'Angelo, O. M. Roscioni, G. Chillemi, S. Della Longa and M. Benfatto, *J. Am. Chem. Soc.*, 2006, **128**, 1853–1858.

79 V. Migliorati, A. Zitolo, G. Chillemi and P. D'Angelo, *ChemPlusChem*, 2012, **77**, 234–239.